STEADY AND UNSTEADY AEROELASTIC SIMULATIONS OF THE HIRENASD WIND TUNNEL EXPERIMENT

Jens Neumann and Markus Ritter

Institute of Aeroelasticity, German Aerospace Center (DLR)
Bunsenstraße 10, 37073 Göttingen, Germany
E-mail: jens.neumann@dlr.de and markus.ritter@dlr.de

Keywords. Steady and Unsteady Computational Aeroelasticity, Fluid-Structure-Interaction (FSI), Transonic and High Reynolds Number Aerodynamics, Harmonic Elastic Motion

Abstract. This paper presents recent results of steady fluid-structure-interaction simulations as well as results of unsteady elastic motion simulations of the HIRENASD (High Reynolds Number Aero-Structural Dynamics) wind tunnel model that were carried out at the Institute of Aeroelasticity in Göttingen. The main objectives of these investigations were the validation of our in-house computational aeroelasticity software for the simulation of fluid structure interaction on the one hand and the computational fluid dynamics solver TAU (development of the DLR) on the other hand against experimental results obtained from the HIRENASD project. With respect to this validation, particular attention was paid to check whether the static deformations of the wing as well as the pressure distribution on the surface of the wing could be predicted correctly. Furthermore, the results of the unsteady simulations were analyzed and validated additionally with respect to the position, the movement and the intensity of the shock evolved on the wing oscillating at high frequencies.

Subsequent to a brief description of the applied numerical methods the simulation models will be presented in detail. The results of the steady aeroelastic simulations at various parameters (angle of attack, flow properties) that were used to validate the coupling algorithms and to show the capability of the correct prediction of deformations and changes in the flow field are presented. Finally, the comparison of any steady and unsteady simulation results with experimental data is presented.

1 INTRODUCTION

Aeroelastic simulations comprise the prediction of both steady and unsteady aeroelastic phenomena. These include e.g. the deformation of wings, stability (flutter, buffet) as well as dynamic response analysis, of e.g. gust loads. While most of the common aeroelastic analysis are performed in the frequency domain, various cases in high-speed flight domains and in regions of large angles of attack can only be analyzed correctly by employing high-fidelity models. These models typically couple structural dynamics (therefore using finite element analysis, FEA) and computational fluid dynamics (CFD). For the handling of industrial configurations, the numerical models are usually set up in well-established and validated disciplinary codes. Static deflections, dynamic stability and response can then be simulated directly using co-simulation among these disciplinary codes. However, for reliable results such an approach requires great attention concerning the set-up of the problem. The obtained results are sensitive to the modeling techniques applied, which comprise mainly the mesh set-up and the numerical schemes (at the CFD part). The proper choice of the spatial coupling scheme is crucial for adequate results as well.

In 2007, the HIRENASD wind tunnel experiment was conducted in the cryogenic European Wind Tunnel (ETW) by RWTH Aachen University and sponsored by the German Research

Association (DFG). The configuration consists of a wing-fuselage model, where the wing was designed with a specified elasticity and fixed with a rigid fuselage at the wind tunnel wall. The main objectives of this experiment were the collection of comprehensive data for the validation of aeroelastic simulation programs on the one hand and to provide a profound insight into the physical phenomena of the flow field at transonic flight conditions at high Reynolds numbers on the other side. Such physical conditions typically occur in flights of large transport aircraft [1], [2].

In this paper the authors present results of time-accurate aeroelastic simulations of selected experimental cases, were dedicated in-house developed coupling software was used. The CFD parts of the coupled simulations were done by the TAU code, a time-accurate, hybrid finite-volume flow solver developed by the DLR. The numerical analysis were performed to accurately predict the non-linear behavior of the flow field in the transonic flow regime at high Reynolds numbers, both for steady and unsteady elastic deformations of the wing model.

Another focus of the investigations was to verify whether the coupling software and especially the flow solver are able to correctly represent the non-linear, unsteady behavior of the flow field occurring at the complex interaction of fluid and structure systems. As a result, the second part of this paper presents simulations employed to compare the results of unsteady aerodynamic response experiments. For this purpose, simulations of elastic wing motions were performed and the obtained pressure distributions have been compared to measured pressure distributions.

2 THE NUMERICAL METHODS USED FOR THE SIMULATIONS

In this section the employed numerical methods of the simulations are described. These methods can be divided in two parts. The first part describes the method for the steady aeroelastic coupling (fluid structure interaction method) using a modal approach. Therein the approach for representing the elastic behavior of the structure as well as the applied interpolation method (which is based on scattered data interpolation with radial basis functions to exchange data on boundaries between the structural and the aerodynamic model) are described. The second part describes the methods applied to the unsteady simulations in order to validate selected, unsteady wind tunnel experiments.

2.1 The Coupling Method for Steady Aeroelastic Simulations

The coupling of aerodynamics, usually represented by a CFD model, and structural dynamics, represented by a FE model, is accomplished via the so called *weak coupling* strategy. At this method the flow solver and the structural solver each integrate their respective governing equations separately. Boundary conditions are exchanged in each iteration step via an interpolation method based on scattered data which becomes necessary due to the different meshes used for each system discretization. This data exchange is carried out as long as a specified convergence criterion is reached. The chosen convergence criterion can e.g. be the minimum of the differences between the last and the actual maximum displacement of a certain point of the structure. In a general and discrete approach, the data exchanged at the system boundaries are the structural displacements on the one hand and the aerodynamic forces on the other hand. These data are exchanged between the flow solver and the structural solver by spatial interpolation. Historically, two coupling strategies evolved that are called *discrete approach* and *modal approach*. They differ in the handling of the degrees of freedom of the system: Either the original degrees of freedom of the structural model are used in a straightforward manner or the system is described by a reduced basis of modal coordinates.

For any steady, coupled aeroelastic simulations presented in this paper the modal approach was used. The associated governing equations and their derivation are described in the following.

The governing equation for a linear elastic structure can be written as

$$\mathrm{K}x = \mathrm{f} \tag{1}$$

where K represents the stiffness matrix of the system, f the vector of the external loads and x the corresponding displacement vector. In the modal approach the structural elasticity is introduced from a modal decomposition of the discrete finite element model, thus leading to a linearly approximated elastic model based on a reduced number of modal degrees of freedom. With the mass-orthogonally scaled modal basis Φ_s, and the generalized coordinates q the physical displacements can be expressed as

$$x_s = \Phi_s q \tag{2}$$

Equation (1) can then be written as

$$\mathrm{K}\Phi_s q = \mathrm{f}_s \tag{3}$$

Multiplying this equation again with the transposed modal basis Φ_s^T leads to

$$\Phi_s^T \mathrm{K} \Phi_s \, q = \Phi_s^T \mathrm{f}_s \tag{4}$$

Due to the mass-orthogonally scaled eigenmodes the expression $\Phi_s^T \mathrm{K} \Phi_s = \mathrm{diag}\left(\varpi^2\right) = \Omega$, equation (4) becomes

$$\Omega q = \Phi_s^T \mathrm{f}_s \tag{5}$$

Assuming that each eigenmode of the structure can be interpolated to the aerodynamic surface via an adequate interpolation method, the interpolated mode shapes of each eigenvalue on the aerodynamic surface can expressed by $\Phi_a = \mathrm{H}\Phi_s$, respectively $\Phi_a^T = \Phi_s^T \mathrm{H}^T = \left(\mathrm{H}\Phi_s\right)^T$. The linear equation (5) then gets the form

$$\begin{aligned} q &= \Omega^{-1} \Phi_s^T \mathrm{f}_s \\ &= \Omega^{-1} \left(\mathrm{H}\Phi_s\right)^T \mathrm{f}_a \\ &= \Omega^{-1} \Phi_a^T \mathrm{f}_a \end{aligned} \tag{6}$$

where f_a now are the aerodynamic forces acting on the aerodynamic surface. The eigenvalues occur in the modal stiffness matrix $\Omega = \mathrm{diag}\left(\omega_1^2, \ldots, \omega_n^2\right)$.

The right hand side of equation (6) shows the equivalence of the explicit back transfer of the aerodynamic forces and a following projection onto the structural eigenmodes to the direct projection of aerodynamic forces onto the individual mode shapes on the aerodynamic surface.

The deformation of the aerodynamic surface is subsequently determined by

$$x_a = \Phi_a q \tag{7}$$

A reasonable number of structural modes must be chosen to represent the dynamic and static behavior appropriately. The structural eigenmodes need to be interpolated on the aerodynamic mesh only once during a pre-processing step. Favourably, this procedure allows convenient handling of free-free structures, since the aerodynamic forces can be split easily in forces acting on rigid-body motions and forces acting on elastic deformations. Additionally, the reduction to low wave number modes filters out local errors in the spatial interpolation. Contrarily to the discrete approach this method is inherently limited to linear structures.

2.2 The Numerical Method for Unsteady Simulations

Besides the necessity to gain a deeper insight in the physics involved in aeroelastic phenomena, the HIRENASD experiment was conducted to obtain data for the validation of methods used for multidisciplinary design and aeroelastic simulations, both steady and unsteady, of airplanes in flight [2]. To get such a comprehensive data base of the dynamic, aeroelastic behavior of the wing model, unsteady elastic motions of the wing were carried out in some of the experiments. Therefore, the wing model was excited in its resonance frequencies in order to respond in its elastic modes. These experiments furthermore yield information about the unsteady behavior of the pressure distribution on the wing surface as well as information about the phase shift between the motion and the response of the flow field, the instantaneous shock position and the amplitude of the shock. For the simulations of these kinds of experiments a simple approach described in the following was used. In the selected experiment for our simulation the second bending mode of the structure was excited. Due to the fact that the measured deformations of this mode were not free from interferences, the corresponding structural mode shape of the finite element model has been interpolated on the aerodynamic surface mesh. Within the unsteady simulations, the elastic motion of the wing has been described by an analytical, harmonic function. For the interpolation of the deflections on the aerodynamic mesh a scattered data interpolation method was applied [3]. In order to simulate the elastic deformation of the wing as accurately as possible, different radial basis functions were tested in a preliminary investigation [4]. In this investigation, the basis functions were tested successively for given analytical form functions that approximate the second harmonic mode shape. The radial basis function that yields the lowest interpolation error (in this case the basis function of the *Thin Plate Spline*) regarding these analytical functions was applied. The interpolated second mode shape of the structure on the aerodynamic surface mesh is depicted in Figure 1.

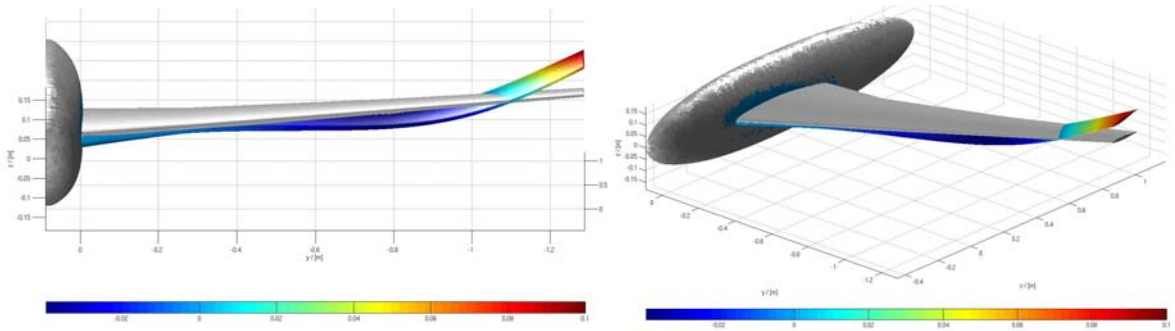

Figure 1: Front and side view of the on the aerodynamic surface interpolated, normalized second mode shape.

For the representation of the unsteady, elastic motion of the wing the aerodynamic surface was deformed following the harmonic equations

$$\begin{aligned} u_x(t) &= \hat{a}\, \Phi_{a,x} \sin(\varpi t) \\ u_y(t) &= \hat{a}\, \Phi_{a,y} \sin(\varpi t) \\ u_z(t) &= \hat{a}\, \Phi_{a,z} \sin(\varpi t) \end{aligned} \tag{8}$$

In equation (8) $u_x(t), u_y(t), u_z(t)$ are the components of the time dependent displacements at each aerodynamic surface point in the corresponding coordinate direction. The vectors $\Phi_{a,x}, \Phi_{a,y}, \Phi_{a,z}$ represent the first or the second eigenmode, respectively, of the structure interpolated on the aerodynamic mesh, which are normalized to a maximum component of one. The value $\hat{a}$ is the maximum displacement amplitude and $\varpi = 2\pi f$ is the respective excitation frequency that is directly obtained from the experimental data. The maximum amplitude in the numeric simulation was calculated from the signal of an acceleration sensor (#15) which is obtained from the experimental data as well. This sensor is positioned near the leading edge at the wing tip. The signal of this sensor is comparatively free from any interferences and its quality is sufficiently good. Assumed that the motion can be approximated as a harmonic function, the displacement of the acceleration sensor #15 was calculated from its signal via equation

$$\hat{a} = \frac{\hat{\ddot{a}}_{15}}{-\varpi^2 \Phi_{a,z,15}} = \frac{\hat{\ddot{a}}_{15}}{-4\pi^2 f^2 \Phi_{a,z,15}} \tag{9}$$

In this equation f denotes the excitation frequency, $\hat{\ddot{a}}_{15}$ the fitted acceleration amplitude of sensor #15 and $\Phi_{a,z,15}$ the value of the interpolated structural eigenmode on the aerodynamic surface in z-direction, located at the same position as sensor #15.

The according reduced frequency of each simulation was calculated using a reference length of the wing chord of $c = 0.3445\text{m}$ (given in [1]). The reduced frequency can then be calculated as follows:

$$\varpi^* = \frac{\varpi c}{v_\infty} = \frac{2\pi f c}{Ma\sqrt{\gamma R T_\infty}} \tag{10}$$

The deformation of the aerodynamic mesh was realised using the TAU mesh deformation tool [5]. Each physical time step the new position of the surface mesh is calculated via equation (8) and the whole volume mesh is deformed by the mesh deformation tool. The mesh velocities are computed via the differences of the last and the current mesh position at each aerodynamic mesh point divided by the actual time step size. All unsteady derivatives are calculated subsequently by the flow solver.

3 THE EMPLOYED FLOW SOLVER

For the steady simulations presented in the following the TAU-Code [6] was coupled with a finite element structural model of the HIRENASD wing. The TAU flow simulation package comprises a finite-volume solver that solves the Reynolds-Averaged Navier-Stokes (RANS) equations on unstructured grids, including several 1- and 2-equation turbulence models as well as LES- and DES models. Additionally, the package includes a pre-processor, a grid

adaptation module and a grid deformation module [5]. Different interfaces to structural analysis software allow coupled simulations of static and dynamic aeroelastic problems. The pre-processing module is used for constructing a dual grid of control volumes from the initial grid which can be composed of tetrahedral, prismatic, hexahedral or pyramidal elements, as well as for partitioning the grid to enable parallel computations. The dual grid contains information about metric data, boundary types and neighbouring domains. The CFD grids were generated using the commercial grid generation software CENTAUR [7].

For the spatial discretization a centered scheme with scalar artificial dissipation was used in combination with both an explicit 3-stage Runge-Kutta scheme and an implicit LUSGS scheme for the temporal integration. For any unsteady simulations a dual time-stepping method was employed, where a multi-grid cycle is used for convergence acceleration on the pseudo time line.

4 USED NUMERICAL MODELS FOR THE HIRENASD WIND TUNNEL MODEL

In the following the used numerical models are described. For the aerodynamic simulation an unstructured grid was build up with CENTAUR. Basis for this model was the original, structured mesh provided by RWTH Aachen University.

4.1 Computational Fluid Dynamics Model

The original computational fluid dynamics model provided by RWTH is a structured multi block mesh with approximately 3.3 million points and 3.2 million cells [8]. For the TAU-Code it was necessary to build up a new CFD mesh in order to use the whole performance of the solver. Therefore, a new mesh was developed based on the geometry of the original mesh. This mesh is shown in Figure 2.

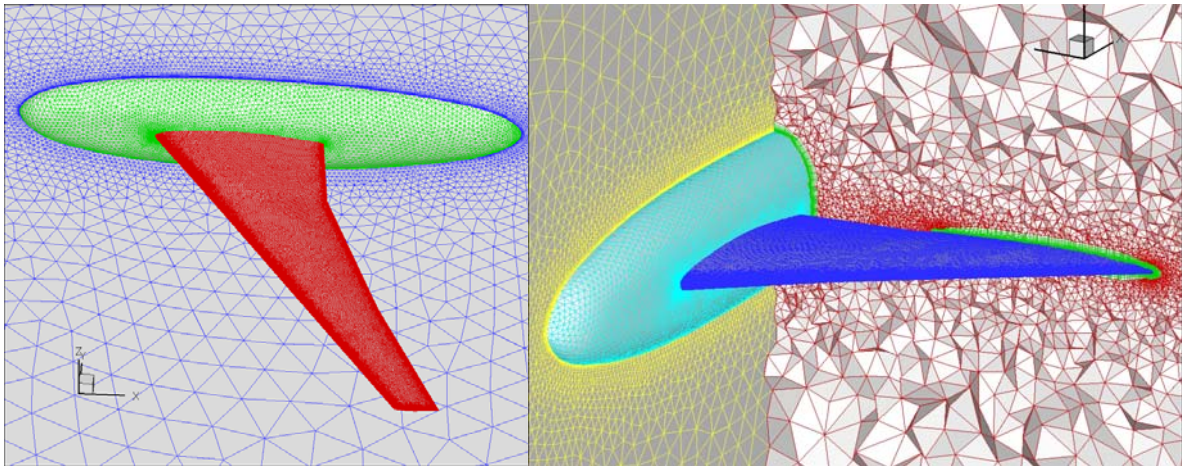

Figure 2: Used CFD model – left whole wing fuselage model, right with tetrahedral elements and boundary layer

The left picture depicts the mesh on the wing surface and the symmetry plane. In the right picture the boundary layer and the volume cells are shown additionally. The thickness of the boundary layer was calculated for a Reynolds number of about 14 million. It contains 30 prismatic layers with an entire thickness of approximately 1.4 % of the mean chord length (0.3445 m). To refine significant regions of the mesh, e.g. the leading and the trailing edge of the wing as well as the wing tip region, so called *geometric sources* were inserted. In the region of the fuselage the sizes of the surface cells were coarsen to limit the number of points of the entire mesh. Relevant properties of the mesh are listed in Table 1.

Number of nodes	Number of total cells	Number of surface cells
~ 5.37 Million	~ 14.18 Million	~ 311000

Table 1 Properties of the deployed CFD mesh.

4.2 Structure Mechanics Model

A usual finite element model build of solid elements with approximately 200.000 nodes provided by RWTH Aachen University was used for the structural discretization of the HIRENASD wing model. This model is depicted in Figure 3. The elastic mode shapes of the model were calculated and used for the coupling process in modal coordinates.

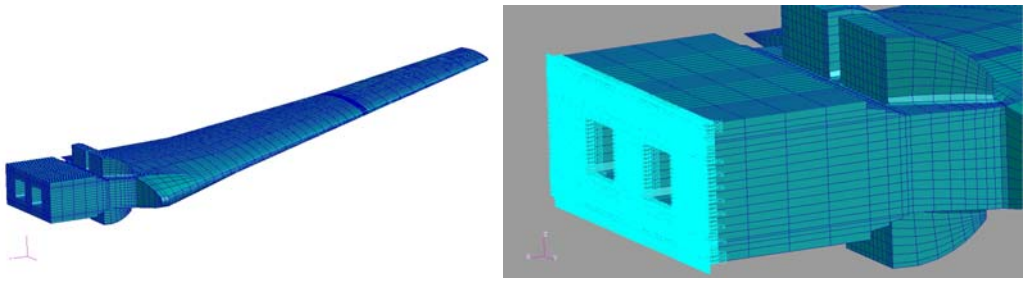

Figure 3: Used finite elements model – left whole wing model, right clamped section.

The model is validated statically and dynamically, this guarantees reliable elastic deformations under aerodynamic loads. Further descriptions of the model and its properties are referred to in [1], [2] and [8].

5 RESULTS

In the following the results of the numerical simulations are presented. At first, steady aeroelastic coupling simulations were performed at transonic flow conditions including strong shocks and large q/E ratio, where significant elastic deformations occurred. The simulation results are compared to data measured at the corresponding experiments. In the second part, the results of the unsteady simulations performed with elastic motions of the wing model are presented. All results are compared to experimental data at specific wind tunnel and model conditions.

5.1 Results of the Steady Aeroelastic Simulations

In this section different steady, aeroelastic coupling simulations at various angles of attack are presented. These simulations were used to validate the coupling algorithms and to show their capabilities of both predicting the correct deformations of an elastic wing supposed to transonic flow and the associated changes in the flow field due to these deformations.

At first two different turbulence models (both the 1-equation Spalart-Allmaras and the 2-equation LEA-k-ω model) were used in the coupled simulations [9]. Since the differences in the simulation results for these two turbulence models emerged as very small, the Spalart-Allmaras model was used in all coupled computations. All steady aeroelastic simulations were performed for a Mach number of 0.80. Consequently, parts of the flow field involve strong shocks due to local supersonic regions. Since interesting transonic flow phenomena and significant wing deformations were found in the experiment at a Mach number of 0.80, a Reynolds number of 14 millions, and a q/E ratio of 0.47e-06, this case was investigated in more detail with various angles of attack (values: -1.0, 0, 1.0, 2.0, and 3.0 degrees).

The results clearly indicate an increasing deformation of the model from the fuselage to the wing. Figure 4 schematically depicts the comparison between the undeformed and the deformed wing for the aeroelastic equilibrium state at an AoA=3.0°. The surface pressure distribution in this plot belongs to the aeroelastic equilibrium state, a relatively strong shock occurs between approximately 20 and 70 percent of the wing span. Furthermore, the deformation of the wing at the tip is shown for the same angle of attack. The maximum deformation at this point reaches 0.0382 meters. Due to the backward swept wing and the aerodynamic loads an additional strong change in the angle of attack of $\Delta\alpha$=-1.21° occurs.

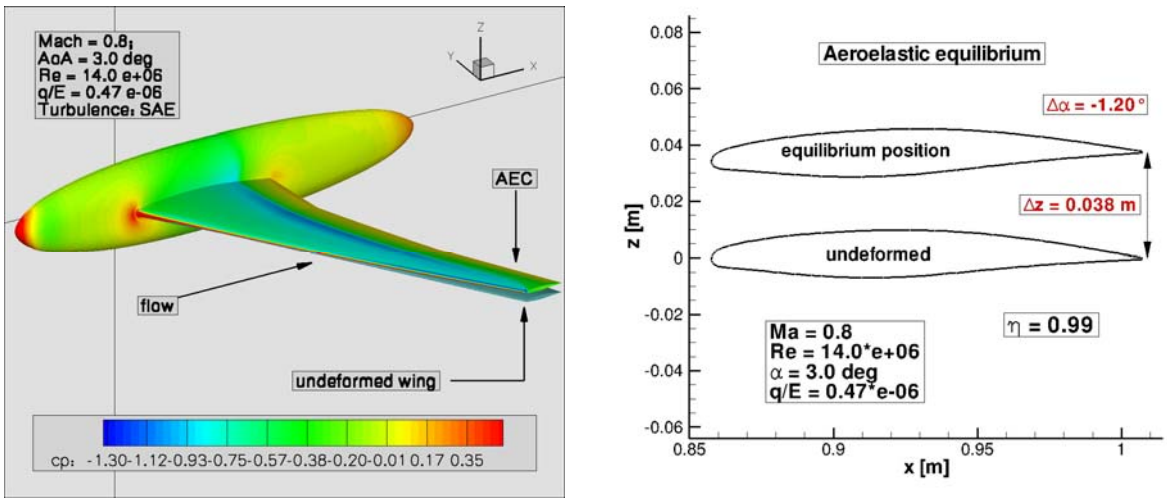

Figure 4: Comparison of jig-shape versus aeroelastic equilibrium of the model at AoA=3.0° and corresponding surface pressure distribution (left). Bending deformation and changes of the angle of attack at the wing tip at η=0.99 and AoA=3° (right).

In Figure 5 the comparisons between measured and calculated bending deformations of the wing for two different angles of attack are shown. In these two cases significant deformations occurred and thus a comparison between the measured and the calculated deformations give a reliable impression of the quality of the numerical simulation concerning the flow field and the interaction with the elastic structure. The numerically calculated wing deformation was compared with the deformations measured at the experiment for angles of attack of 2.0° (left) and 3.0° (right).

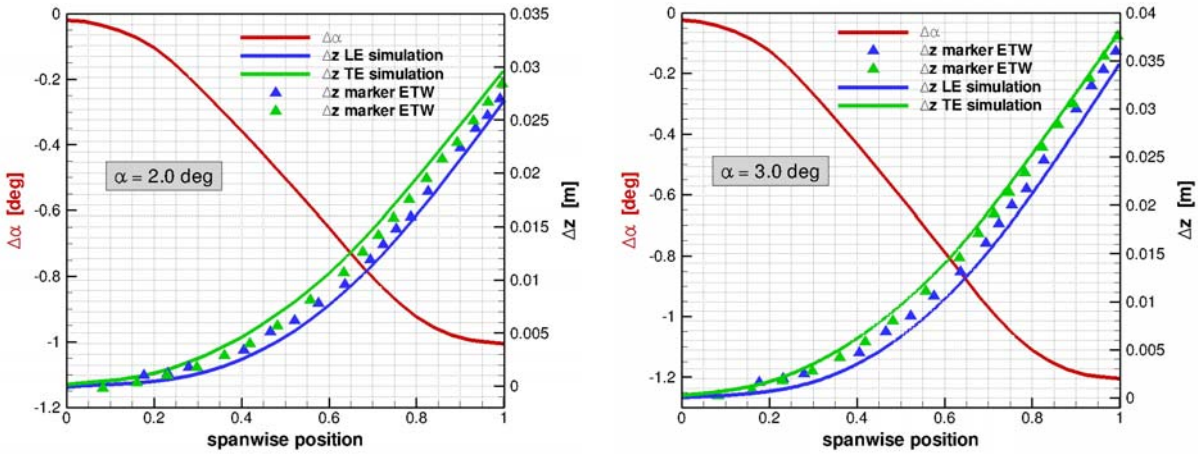

Figure 5: Deformation of the leading and the trailing edge and changes in the AoA along the wing span for case AoA=2.0 degree (left) and AoA=3.0 degree (right).

The numerically calculated elastic deformation for an AoA=2.0° fits excellently the measured data on the entire wing, both at the leading edge and the trailing edge. The bandwidth of the leading and the trailing edge deformations of the simulation encloses any of the measured deformations. It should be mentioned that any markers are positioned in the region between the leading and the trailing edge of the wing surface. The same statement can be given for an AoA=3.0°, the good correlation between the simulation and the experimental results is clearly noticeable. The distribution of the twist angle is plotted additionally in Figure 5.

For the variation of the angle of attack all calculated maximum deformations at the leading and the trailing edge at the wing tip (η=1.0) as well as the maximum changes in angle of attack (torsion angle) at the same position are listed in Table 2.

α [deg]	Δz_{LE} [mm]	Δz_{TE} [mm]	Δα [deg]
-1.0	5.82	6.83	-0.36
0.0	12.6	14.2	-0.57
1.0	19.8	22.0	-0.79
2.0	26.8	29.7	-1.01
3.0	34.8	38.2	-1.21

Table 2: Simulation results of discrete displacements at the leading and the trailing edge of the wing as well as the wing twist both at η = 1.0 (wing tip).

In Figure 6 the dimensionless pressure coefficient (cp) is shown for all simulations. Each row depicts the results of three different cut planes. The first cut plane is located at 14%, the second one at 46%, and the third one at 95% the of the wing span. The angle of attack varies between -1.0 and 3.0 degrees. The results of the jig shape and the deformed shape compared to the pressure coefficients of the experiment are shown.

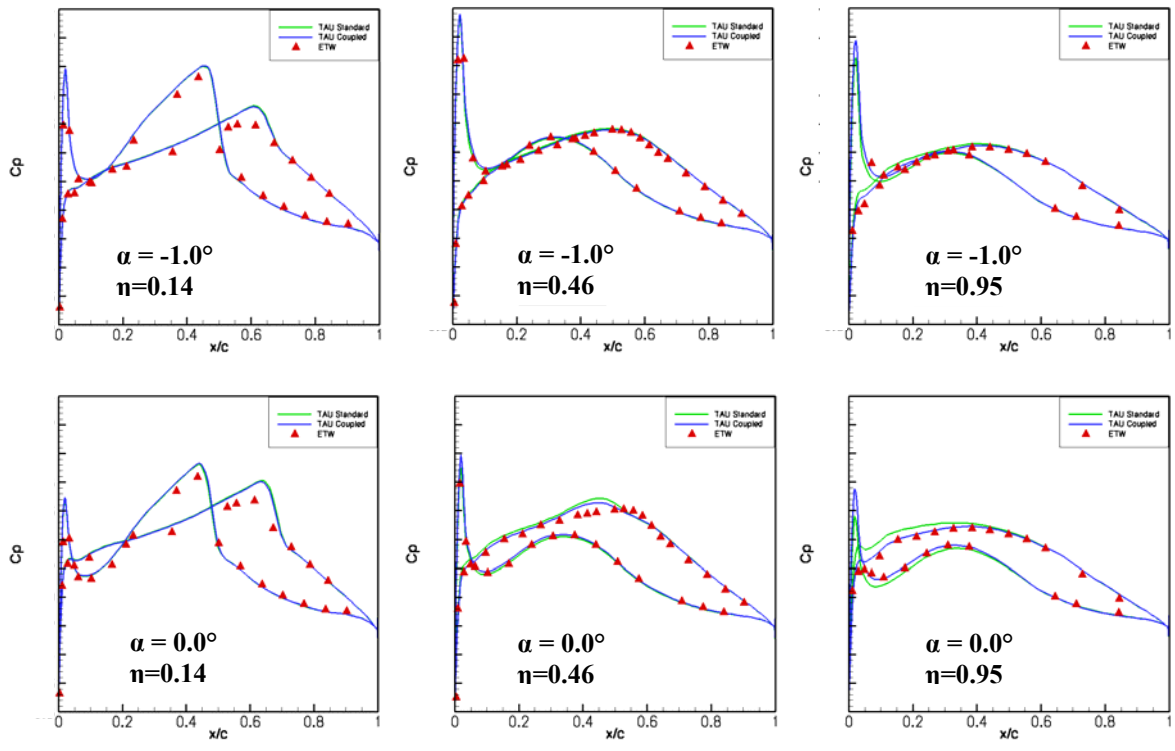

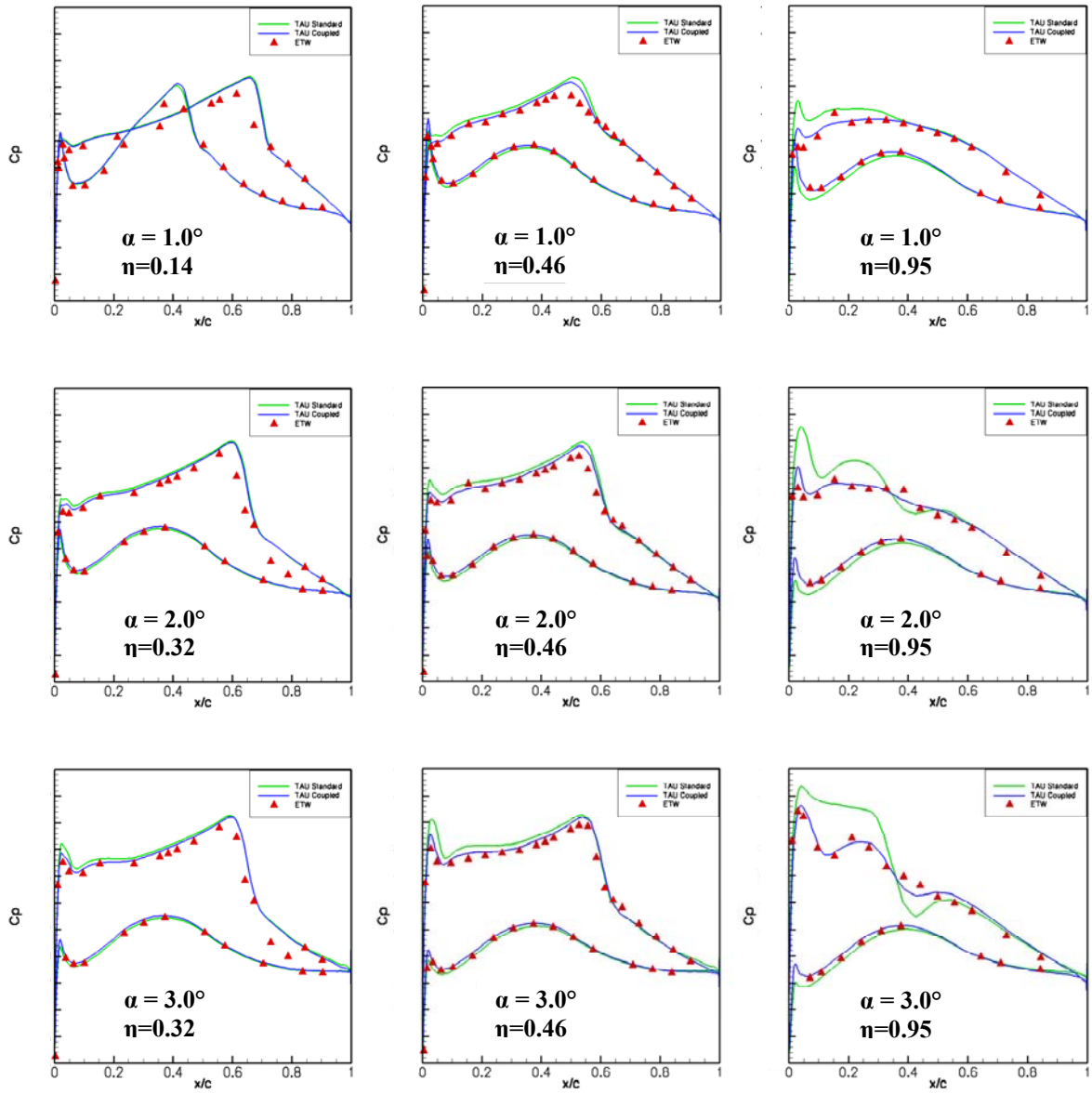

Figure 6: Comparison of experimental and simulated (coupled simulation) pressure coefficients at different sections of the wing (cut planes located at η=0.32, 0.46 and 0.95). The green lines depict the cp values for the jig shape, the blue lines the coupled solution and the triangles the measured data. Flow parameters: Re=14e+06, Ma=0.8, q/E=0.47e-06. Angles of attack: -1.0, 0, 1.0, 2.0, and 3.0°.

Regarding the lowest angle of attack (-1.0 degrees), the influence of the elasticity of the wing becomes almost zero (this angle is close to the zero-lift angle). The simulated pressure values fit well with the measured ones. The suction peak at the upper side of the leading edge is reflected well by the simulation in all sections. Also the increase of the pressure on the lower side on the wing is predicted well. A low influence of the elastic deformation regarding the pressure coefficients can be observed beginning at an angle of AoA=0.0° at the outer section of the wing (η=0.95). This influence increases as the angle of attack increases. From an angle of attack in the region of 2.0° up to 3.0° it becomes evident that the deformation of the wing strongly influences the resulting pressure distributions. Mainly at higher angles of attack the differences in the outer sections of the wing between the jig-shape results and the aeroelastic simulations show the strong effect of the elasticity: increasing the angle of attack yields an increase of loads and thus an increase of deformation. In turn, a reduction of the local angle of

attack at the wing tip is followed by a local lift reduction in this section. The position of the shocks at higher angles of attack in the middle part of the wing could be predicted satisfyingly, as well as the pressure decrease due to the deformation of the wing and a change of the angle of attack in the outer sections.

Figure 7 depicts the convergence behavior of the aerodynamic coefficients during the coupling process exemplarily for an AoA=2.0° and AoA=3.0°. The lift and the moment coefficients show convergence after ca. 15000 iterations.

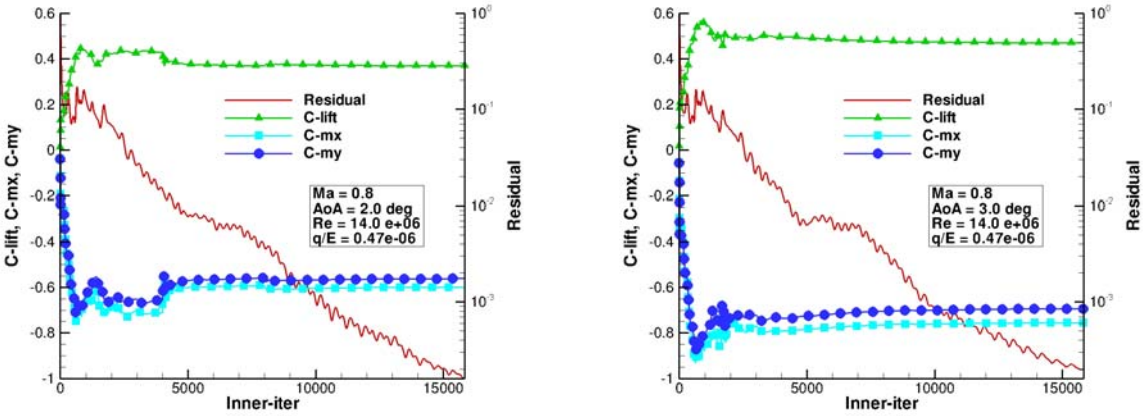

Figure 7: Convergence history of residual, c-lift, c-mx and c-my for a coupled simulation at AoA = 2.0° (left) and AoA = 3.0° (right).

In conclusion, it can be pointed out that the results presented above show that the steady coupling process chain with TAU can be used as a reliable tool for high-fidelity simulations of weak fluid-structure-interaction problems. Both the flow field and elastic deformations of the wing are reflected correctly. Also the experimental data of the HIRENASD wind tunnel experiment are well suited to verify numerical methods for steady fluid structure interaction simulations.

6 Results of the Unsteady Aeroelastic Simulations

In [9] a first dynamic aeroelastic coupling with the HIRENASD wing model was performed. The objective thereby was to show the capabilities of the coupling procedure concerning the simulation of transient aeroelastic behavior of the wing by using a CFD-code for complex transonic flow and a FE-code for the elastic properties of the wing. In the next step, the dynamic behavior of the transonic flow around the wing under transient elastic deformations of the wing at high frequency was investigated more detailed and compared to experimental results. Therefore, the wing was excited in its second eigenmode at a frequency of 78.9 Hz. The simulation was conducted as explained in section 2.2. As described in chapter (2.2), the second eigenmode of the structural model of the wing was used to represent the deformation of the wing in the simulation. Therefore, the CFD mesh is deformed appropriately each physical step during the simulation using the mesh deformation module provided by TAU. Mostly, one oscillation period of the wing was sub-divided into 180 steps, resulting in a physical time step of ca. 7e-5 seconds for a frequency of 78.9 Hz. Subsequent to the CFD simulation, a FFT analysis of the results (were only the first harmonic of the results was taken into account) was accomplished to gain the relevant data of the unsteady flow field: The magnitudes as well as the respective phase angles of the cp values.

Any unsteady data of the HIRENASD experiment are available as time-series. Unfortunately, the raw data appear quite noisy and thus an adequate postprocessing (filtering) is essential. It must be remarked that the Signal-to Noise-Ratio (SNR) of the experimental data turned out to be comparatively low with values ranging from ca. 6dB at the trailing edge of the wing to ca. 15 dB at its leading edge. The magnitude and the phase angle of the pressure values are obtained by applying a transfer function to the filtered raw data. These transfer functions were derived each such that it specifies the correlation between the unsteady signal of a certain cp sensor and the unsteady displacement of a designated point on the wing surface (here the wing tip trailing edge was used). The data of interest (cp magnitude and the phase angle of every pressure sensor signal) are now calculated directly from the respective transfer function.

Each unsteady simulation is based on a steady initial solution. Therefore, an aeroelastic equilibrium state was calculated via the coupling procedure from section 2.1. The physical properties for the two flow conditions steady and unsteady are listed in Table 3.

Description	**Value**
Mach number [-]	0.80
Reynolds number [-]	7.0e+06
q/E ratio [-]	0.22e-06
Angle of attack [deg]	1.50
Exiting frequency [Hz]	78.9
Max. Amplitude [m]	3.9e-03
Reduced frequency [-]	0.66
Mode shape	Second bending mode

Table 3: Physical properties from the experiment (also used as input parameter for the steady and unsteady simulations).

In Figure 8 the steady pressure coefficients of the three cut planes located at 32, 66, and 95% of the wing span are depicted for the undeformed simulation, the aeroelastic equilibrium state, and the experimental data. It can be observed that the solution of the aeroelastic equilibrium state fits the experimental data better than the solution of the undeformed mesh in the outer section at η=0.95 does. This behavior arises due to the elastic deformation of Δz=0.013 meter at the wing tip. This deformation decreases the effective local angle of attack; the result is a decrease of the local pressure coefficients. The position of the shock in the inner region of the wing could not be predicted correctly, recognizable in the left plot of Figure 8. Though the data fit well at the outer cut planes, in this region the highest deformations of the wing were expected.

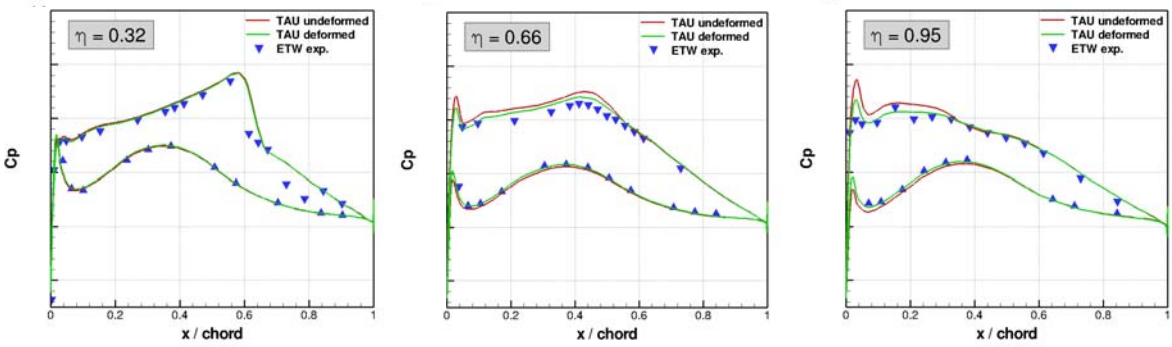

Figure 8: Steady pressure coefficients of the undeformed state, the aeroelastic equilibrium state, and the experimental data (cut planes located at η=0.32/0.66/0.95).

After the calculation of the initial states the unsteady simulations with the wing oscillating at a specified frequency were performed. Here, six periods of the harmonic motion for the second bending mode at 78.9 Hz. were calculated with 180 time steps for each period. For each time step a maximum of 100 inner iterations and a minimum residual of 1e-04 were set to get a converged solution, but also to limit the calculation time. In Figure 9 the changes in the pressure coefficients around the steady pressure distributions are shown for three cut planes (η=0.46/0.66/0.8). The maximum amplitudes of the changes in the pressure distribution occur both at the 0.46 and the outer section of the wing in the region of the shock.

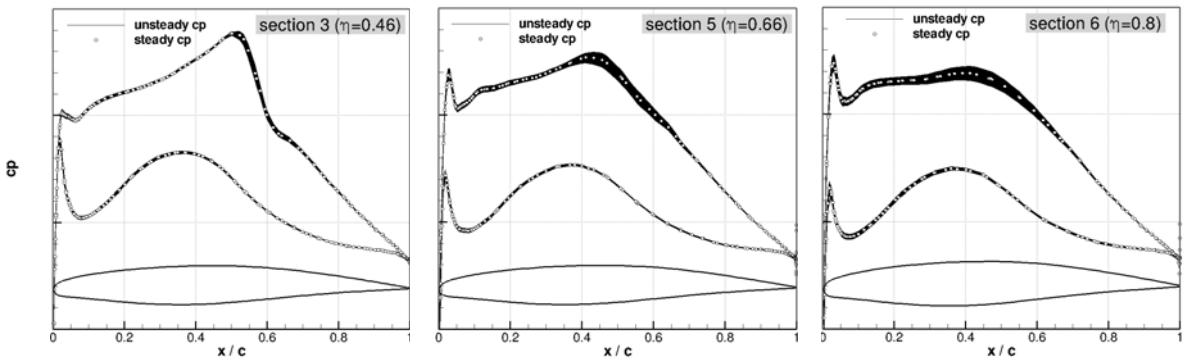

Figure 9: Steady and unsteady pressure coefficients cp for the second mode shape. Harmonic oscillation at a reduced frequency of $\varpi^* = 0.66$ (cut planes located at η=0.46/0.66/0.8).

Both the simulated unsteady pressure coefficients and the measured ones have been transformed properly using an FFT analysis. The results for the magnitude and the phase angle of the pressure coefficients are depicted in Figure 10. The lines in the plots represent the simulation and the symbols the experimental data. It can be seen that the calculated and the measured magnitude in cut plane η=0.46 fit well. Especially at the position of the shock the calculated unsteady changes in the pressure agree quite well with the measured ones. That is also the case for the phase shift in that cut plane. The strong increase of the phase shift around the shock appears in the simulation nearly at the same position as in the experiment. Behind the shock the phase shift between the movement of the wing and the reaction of the pressure coefficients reaches a value of almost 180 degrees. The phase shift increases in the direction of the wing tip up to nearly 360 degrees. Furthermore, one can observe that in direction of the wing tip (see cut planes at η=0.59/0.66/0.8) the magnitude of the unsteady pressure decreases in comparison to the experiment. However, the influence region of the unsteady pressure in the simulation is enhanced compared to the influence region of the experiment. The strength of the unsteady variations surrounding the shock is much stronger in the simulation than in the experiment. The magnitude of the simulated cp values is decreasing when compared to the experimental values, while the phase shift from the simulation moves towards the trailing edge compared to the experiment. One explanation therefore could be the mesh resolution in that region. While the mesh is finer in the inner region of the wing (η=0.46), it becomes coarser in direction towards the wing tip. Probably the changes of the unsteady flow properties get to strong due to the coarser mesh in downstream direction. That can also be explained if the leading edge for all cut planes is considered. In this region the mesh resolution is rather fine and thus the suction peak and its changes are always predicted well. The prediction of the magnitude and the phase angle of the pressure coefficients on the lower side are very close to the experimental data in all cut planes. Finally, it should be mentioned that these results were obtained within a first investigation of these kinds of unsteady experiments. Further simulations and validations of unsteady data will follow in the future

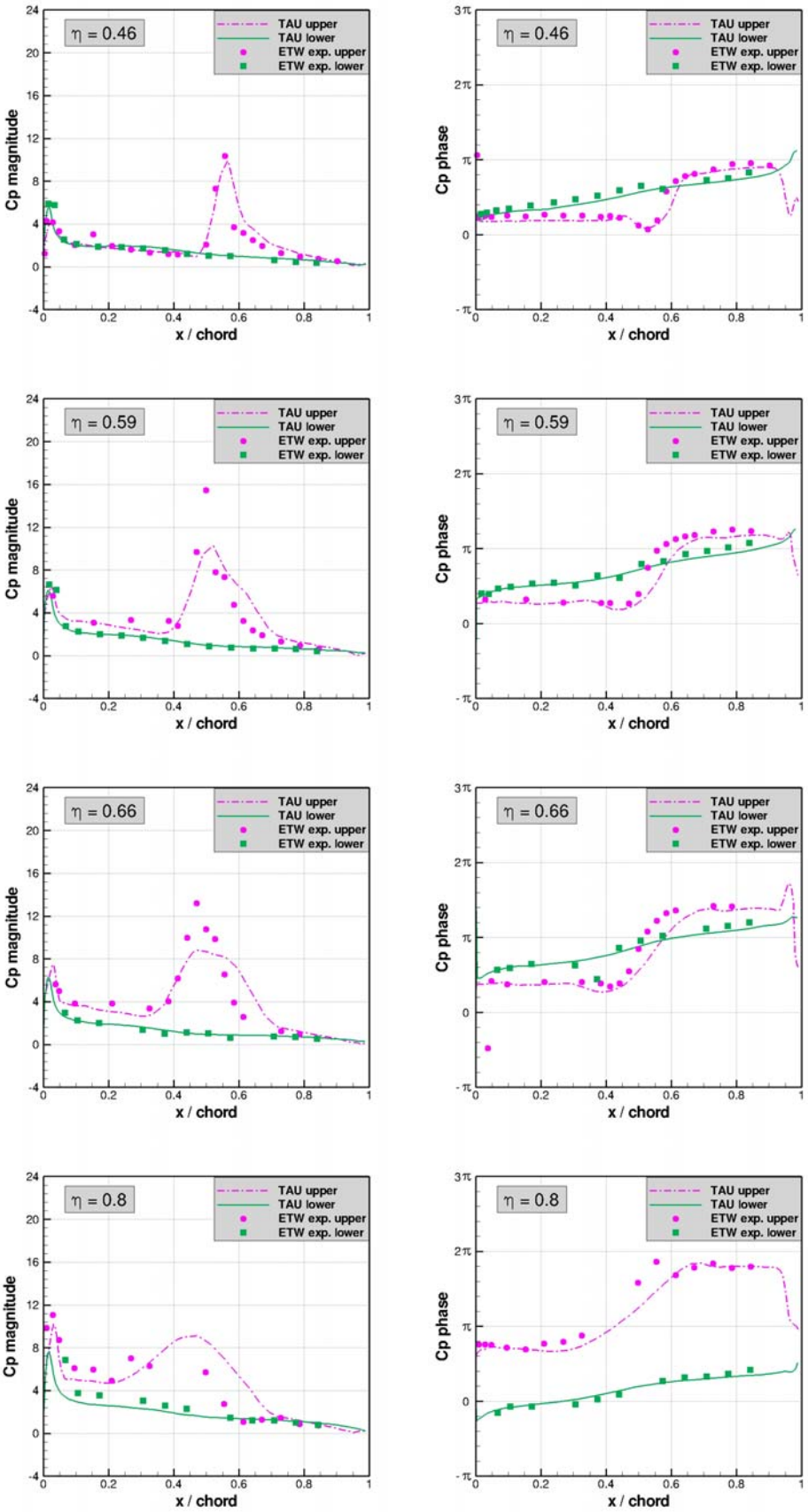

Figure 10: Magnitude and phase shift of the unsteady pressure coefficients cp for the second mode shape (cut planes located at η=0.46/0.59/0.66/0.8).

7 CONCLUSION AND OUTLOOK

In this paper numerical results for steady and unsteady simulations of the HIRENASD wind tunnel experiment are presented. In comparison with the experimental data, we partly got very good numerical results for steady aeroelastic analyses using the described coupling method. The pressure coefficients, displacements and changes in the local angle of attack (twist of the wing) can be predicted precisely. The employed flow solver TAU, the numerical models and their model resolution as well as the introduced coupling method are able to give a correct prediction of transonic flow phenomena like shock position in interaction with the elastic wing model. The results of the unsteady simulations regarding the harmonic oscillation within the second bending mode of the wing model partly show very good agreement concerning the magnitude and the phase shift. Regarding these first investigations, the TAU-Code predicts the unsteady behavior of transonic flows on the elastically deformed wing in a satisfying manner. The results of the unsteady experiments of the HIRENASD wing can also be used for the validation of unsteady flow simulations. Questions remain regarding the improvement of the simulation results, both steady and unsteady. For simulations in the future, further investigations under consideration of these experiments should be carried out. First of all, a mesh convergence study should indicate whether the results become better due to e.g. a refinement of the mesh in the outer region and especially in the shock regions.

8 REFERENCES

[1] Ballmann, J., Dafnis, A., et al. (2006). *The HIRENASD Project: High Reynolds Number Aerostructural Dynamics Experiments in the European Transonic Windtunnel (ETW).* International Council of the Aeronautical Sciences (ICAS) Congress, Paper 2006-5.11.2, Hamburg.

[2] Ballmann, J., Dafnis A., Korsch, H., et al. (2008). *Experimental Analysis of High Reynolds Number Aero-Structural Dynamics in ETW.* American Institute of Aeronautics and Astronautics Paper 2008-841, 46th AIAA Aerospace Science Meeting and Exhibit, January 7-10, 2008, Reno, Nevada.

[3] Beckert, A., Wendland, H. (2001). *Multivariate Interpolation for Fluid-Structure-Interaction Problems using Radial Basis Functions*. Aerospace Science and Technology, Art. No. 5125.

[4] Neumann, J. (2008). *Identifikation radialer Basisfunktionen zur räumlichen Strömungs-Struktur-Kopplung unter Berücksichtigung des Interpolations- und des Lasttransformationsfehlers.* DLR-IB, IB 232-2008-J01, Deutsches Zentrum für Luft- und Raumfahrt, Göttingen, Germany.

[5] Gerhold, T.; Neumann, J. (2006). *The parallel mesh deformation of the DLR TAU-Code.* 15. DGLR-Fach-Symposium der STAB, Nr. 2006-11-29-2006-12-01, Darmstadt, Germany.

[6] Gerhold, T., Galle, M., Friedrich, O., Evans, J. (1997). *Calculation of Complex Three-Dimensional Configurations Employing the DLR-TAU Code.* AIAA Paper 97-0167.

[7] CentaurSoft, CENTAUR, http://www.centaursoft.com.

[8] Reimer, L., Braun, C., Chen, B.-H., Ballmann, J. (2007). *Computational Aeroelastic Design and Analysis of the HIRENASD Wind Tunnel Wing Model and Tests.* IFASD.

[9] Dolle, T.J.A. *Numerical aeroelastic simulations on the HIRENASD wind tunnel model.* DLR-IB, IB 232-2008-C04, Deutsches Zentrum für Luft- und Raumfahrt, Göttingen, Germany.

[10] Neumann, J., Nitzsche, J., Voss, R. (2008). *Aeroelastic Analysis by Coupled Non-linear Time Domain Simulation.* RTO-AVT-154, Specialist's Meeting on Advanced Aeroelasticity, Loen, Norway.